Threshold studies of a multivacancy process in the $K\beta$ region of argon

R. D. Deslattes, R. E. LaVilla, P. L. Cowan, and A. Henins
Quantum Metrology Group, National Bureau of Standards, Washington, D.C. 20234
(Received 26 July 1982)

Threshold-region measurements are reported for the production of single-vacancy and multiple-vacancy configurations of atomic argon by monochromatic x-ray photons in the region of the 1*s* ionization threshold. The experiment used monochromatized synchrotron radiation produced in the six-pole wiggler at the Stanford Synchrotron Radiation Laboratory with 3.2-GeV electrons at circulating currents of 20—30 mA. Secondary radiation including elastically and inelastically scattered radiation as well as fluorescent spectra were analyzed in a focusing spectrometer with a linear position-sensitive detector. Fluorescent spectra in the $K\beta$ region were modeled by inclusion of spontaneous decay of double-vacancy configurations of the type $KM \rightarrow M^2$. This multiplet model permitted extraction of partial cross sections for the production of KM_{I} and $KM_{\mathrm{II,III}}$ configurations. This report also contains new data on details of absorption fine structure in the region of the single-vacancy threshold and the principal double-vacancy thresholds.

I. INTRODUCTION

Observed x-ray emission spectra excited far above a single-vacancy threshold energy show both single- and multiple-vacancy features. While these may be plausibly disentangled in simple systems by theoretical estimates and appeals to obvious empirical regularities, such analyses are not practical for systems having an interesting level of complexity. Similarly, there are features found in the absorption spectra of even monatomic gases which are apparently associated with energetic thresholds for opening of channels to multiple-vacancy configurations which are the initial states for many satellite emission features.

Study of the threshold behavior of x-ray emission spectra excited by tunable x radiation provides an opportunity to correlate the effects of multiple-vacancy processes in emission and absorption spectra. An additional result of such a study is the threshold behavior of the partial cross section for a production of particular double-vacancy configurations. Such data are interesting at the present time since near threshold the standard "shake" model for multiple-vacancy production becomes inappropriate. More fundamental calculations which are now becoming available for simple systems may also be tested against our data.

Our initial study is of the $K\beta$ region of atomic argon excited by monochromatic x rays tunable through the region of single-vacancy (K) and double-vacancy (KM) production. The secondary (fluorescent) radiation, excited by monochromatized synchrotron radiation, was analyzed by a high-resolution focusing spectrometer with an imaging detector. In this same study, data were obtained on the $K\alpha$ region and on elastic and inelastic scattering cross sections, but those results will be reported elsewhere. The present report focuses on $K\beta$ fluorescence while describing in some detail the experimental arrangements common to the three subjects. Incidental to this emission study we obtained new data on the general behavior of the photoabsorption spectrum throughout the K region.

Results to be reported here are both richer in detail than we anticipated and afflicted by several difficulties which are not intrinsic. They thus suggest a need for further measurements which are currently awaiting final construction of new instrumentation. Nevertheless, the data which are at hand speak with considerable clarity. In the concluding section we discuss follow-on measurements of the spectroscopy of atomic gases and of more complex systems.

II. GENERAL FEATURES OF THE SPECTRA

Figure 1 is the K threshold absorption spectrum (as obtained in the present investigation) together with an emission spectrum of $K\beta_{1,3}$ and its principal high-energy satellites β^V and β''. This emission spectrum was excited by 10-keV electron bombardment of argon flowing from a gas jet.[1] The main features of the absorption spectrum are the (partly visible) Rydberg series $1s \rightarrow np$ $(n \geq 4)$ (A) together with an adjacent continuum, as were described by

 ©1983 The American Physical Society

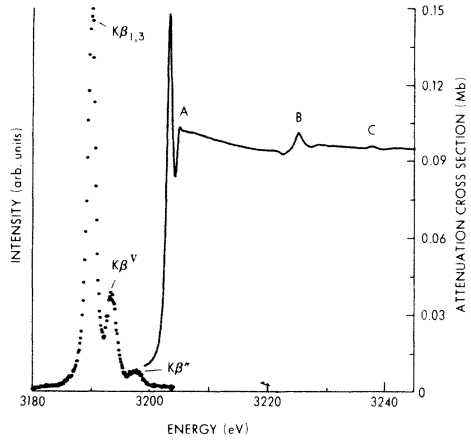

FIG. 1. Argon emission and absorption vs energy. Ar $K\beta$ emission (circles) was stimulated by 10-kV electron bombardment. The Ar K-edge absorption spectrum (solid line) was obtained at SSRL.

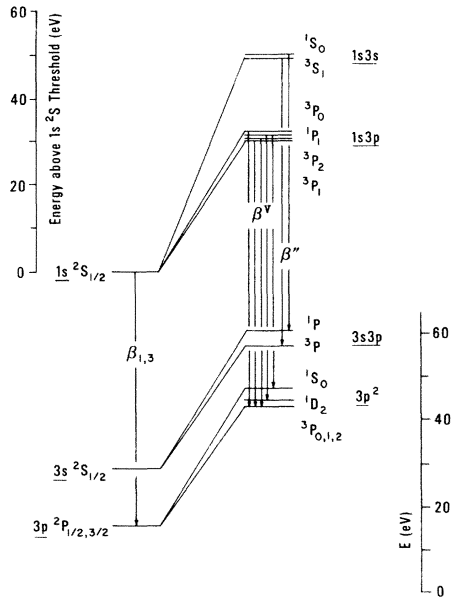

FIG. 2. Diagram of principal argon single- (left) and double- (right) vacancy transitions expected to produce x-ray emission near $K\beta$ energy, using the calculated values from Ref. 11 for initial states and tabulated values in Ref. 12 for the final states.

Parratt in 1939 (Ref. 2) and later by Brogren.[3] More detailed modeling and data fitting[4] have not perturbed Parratt's analysis noticeably but have served to locate the beginning of the continuum 2.70 eV above the first ($4p$) resonance. A subsequent feature (B) $\sim$22 eV above the main resonance was first seen in absorption by Schnopper[5] and later by Bonnelle and Wuilleumier[6,7] who also reported the second piece of structure about 12 eV higher (C). From energy considerations alone it is natural to associate these two structures with opening of channels leading to $KM_{\mathrm{II,III}}$ and KM_{I} double-vacancy configurations as was done in Refs. 5 and 7. A recent report by Hastings and Eisenberger who used synchrotron radiation[8] showed the structures in greater detail and revealed shapes suggestive of the "Fano profiles" that are characteristic of interference between quasibound levels and degenerate continua. As will be seen below, our data reveal these structures in still greater detail and encourage us to offer more specific interpretation than has been previously attempted. In addition, we hope that the availability of this spectrum will encourage more definitive calculations.

An earlier study of the emission spectrum was carried out by one of the present authors who used fluorescence excitation from a conventional x-ray source.[9] Analysis in Ref. 9 was carried out using hints from an "isoelectronic" sequence together with crude wave functions.[10] It was suggested that the main processes responsible for the emission spectrum were as indicated in Fig. 2. The double-vacancy terms indicated are shifted from the single-vacancy terms by the direct part of the Coulomb interaction and split, in the usual way, by the exchange energy. Such a diagram is appropriate only in the case of an initially closed-shell atom. Presence of an open shell (besides those associated with specific inner- and outer-shell vacancies) leads to considerably more complex term arrays in both the initial and final states. Identification of the strong line was retained as the unresolved doublet $\underline{1s}^2S_{1/2}\rightarrow\underline{3p},^2P_{1/2,3/2}$ (hole states are underlined), i.e., $K\rightarrow M_{\mathrm{II}},M_{\mathrm{III}}$. The principal satellite group β^V was suggested to arise from transitions involving double-vacancy configurations of the form $\underline{1s}\,\underline{3p}\,^{1,3}P\rightarrow\underline{3p}^2\,^1S\,^3P\,^1D$ ($KM_{\mathrm{II,III}}$ to double M-shell vacancies in various combinations). The origin of $K\beta''$ was not unambiguous at that time and its apparent lack of structure was puzzling.

III. EXPERIMENTAL APPARATUS

The measurement program we are reporting depends on both an intense source of radiation and efficient utilization of the secondary spectra. It will thus appear in what follows that we required a high flux ($\sim 10^{12}$ photon/sec) source of tunable, monochromatic x rays, implying a high-energy electron storage ring source with wiggler enhancement. Furthermore, an imaging spectrometer was developed yielding a significant multiplex advantage in the acquisition of secondary spectra.

Our measurements were carried out at the Stan-

ford Synchrotron Radiation Laboratory during dedicated operation of the electron storage ring SPEAR.[13] The stored electron current was in the range 20—80 mA at a nominal energy of 3.2 GeV. We used radiation produced by a six-pole transverse wiggler[14] operated at a magnetic field of 1.1 T (11.2 kG).

The incident radiation was monochromatized (with an effective resolution near 1 eV) by a separated function focusing two-crystal monochromator as described by Hastings *et al.*[15] The initial optical element was a mirror adjusted to produce a focus in the sample region. The two Si(111) crystals were separately mounted and aligned in the monochromator. Additional adjustment of the crystals was occasionally required due to varying heat load on the first crystal from the incident radiation (see Sec. IV for further discussion). Incident and transmitted radiation monitors, together with the sample cell, were contained in a single aluminum housing (see Fig. 3). A Be window separated the helium in the primary monochromator beamline from the helium supplied to the ion chambers. The sample cell (path of 1.0 cm) contained flowing argon gas at 5×10^4 Pa (0.5 atm) and was separated from the monitor helium gas by two other Be windows and from the vacuum of the secondary monochromator by a third Be window. All Be windows were 25 μm thick. The preamplified ionization chamber currents were converted from voltage to frequency, then integrated by counters.

For the secondary spectrometer we combined a singly bent Si(111) crystal with a radius of 2 m with a linear position-sensitive proportional counter to produce synoptic imaging of a small spectral region centered around the $K\beta_{1,3}$ emission feature. The entire structure was simply assembled from two pieces of vacuum piping joined by a trapezoidal block which contained the crystal as is shown in Fig. 3.

The position-sensitive proportional counter was of the backgammon variety as described by Allemand

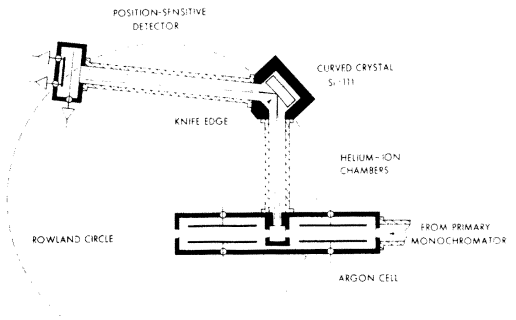

FIG. 3. Schematic of sample chamber and secondary spectrometer.

and Thomas.[16] Hybrid charge sensitive preamplifiers[17] were affixed directly to the counter body and subsequent signals processed after postamplification in the usual way by an analog dividing circuit.[18] Gating of the analog dividing circuit was determined by the output of a single-channel analyzer which examined pulses produced on the counter's center wire. The counter was operated at a pressure of approximately 5×10^4 Pa (0.5 atm) with a quasistatic fill of xenon-methane (90-10). Under the conditions of our operation, performance of the counter deteriorated slowly so that daily evacuation and refill sufficed to ensure optimum operation. Output from the analog divider circuit was accumulated in a multichannel analyzer whose contents were periodically transferred to flexible magnetic disks.

IV. DESIGN OF MEASUREMENTS

From the overview given above of emission satellites and suprathreshold structures in absorption emerge several expectations. First, incident photons with energies greater than the single-vacancy threshold but less than double-vacancy thresholds should stimulate fluorescence of the parent line but not satellites. Specifically, if the emission satellite structure $K\beta^V$ is indeed due to the process $KM\rightarrow M^2$, then photons having energies E such that $E(K)<E<E(KM)$ should produce $K\beta_{1,3}$ fluorescence but not the $K\beta^V$ satellite. Secondly, if the extra absorption features are indeed also associated with opening of channels leading to multiple-vacancy initial states, then the onset of the satellites due to multiple vacancies should closely correlate with tuning of the incident photon energy through these features. Furthermore, if there is a satellite such as $K\beta''$ whose origin is not clear, finding its excitation threshold is likely to be helpful in narrowing the range of possibilities. Also, as suggested above, since the photoproduction of double vacancies is now calculable, data on the energy dependence of appropriate partial cross sections (as obtained from the energy dependence of satellite to parent intensity ratios) is of current interest. Finally, subshell thresholds might also be resolved with a corresponding elucidation of the multiplet character of $K\beta^V$.

An unforeseen factor affecting our measurement strategy was the presence of serious instabilities in the primary monochromator. These were primarily caused by heating of the first crystal and the focusing mirror as well as changes in location of the source following each reinjection of SPEAR. Our strategy for dealing with this problem involved frequent rescanning of the absorption spectrum and subsequent relocation of the primary monochroma-

tor setting for a specified excitation energy. On the one hand, these frequent spectral sweeps gave us some new results on absorption structures (reported next, below) while on the other hand, they were insufficient to permit concordance of all emission data. Fortunately, for incident energies within 30 eV of the $K\beta$ fluorescence, elastically scattered photons fell within the acceptance range of the secondary spectrometer providing convenient markers.

We present below (Sec. V) the results of absorption scans and then, in the following section (Sec. VI), sample emission spectra obtained at several excitation energies as well as excitation functions and threshold energies for those components into which we think the spectral profiles can plausibly be resolved.

V. THE ABSORPTION SPECTRUM

As was noted above, our measurements were carried out with high photon flux incident on the sample, and there was need to frequently rescan the absorption spectrum to account for drifts in the primary monochromator. These circumstances led to an accumulation of data on the absorption profile having excellent statistics both as regards individual observational variance and a large number of measurement replications. The results provide a more detailed view of the absorption spectrum than was previously available.

To gain an overview of the argon K absorption edge, the measured absolute absorption edge attenuation cross section versus energy is shown in Fig. 4. Detailed scans were obtained in the vicinity of expected thresholds with additional isolated points spanning the incident energies from 3125 to 4500 eV. The individual data points represent average absorption during periods of up to several hours (during collection of emission spectra), whereas the absorption scans were accumulated in a few minutes. Thus the increased scatter of the isolated points relative to the data from scanned energies reflects the thermal problems and electron-beam drift mentioned earlier.

For comparison, Fig. 4 also shows the theoretical photoabsorption cross section versus energy calculated by the hydrogenic approximation[19] including quadrupole and octopole terms.[20] Although the hydrogenic approximation is not expected to be reliable for cross sections at energies below 10 keV,[21] it does provide a convenient basis for comparison of theory and experiment. As previously found by Wuilleumier, the experiment and simple theory are in general quantitative agreement above the K edge.[7] However, we would like to point out two marked qualitative differences. First, the sharply peaked resonance features above the K edge, which have already been mentioned, and secondly, the significantly greater slope of the experimental curve near threshold. This latter effect is particularly evident between 3206 and 3225 eV, where the experimental cross section drops much more steeply than theory. This behavior was also evident in the earlier studies but was not discussed.[5]

The region below 3206 eV contains the well-known resonances associated with the $1s np$, $n \geq 4$ Rydberg states. The limiting value of this series estimated in the $Z+1$ approximation[2-4] or, equivalently, by a quantum-defect procedure,[22] lies at 3206.0 eV. At the series limit one can place an arctangent component intended to describe transitions to the free-electron continuum. Such a model fits locally but would probably not be sustained by a more rigorous analysis that would take into account the slope immediately above the threshold.

Some recent atomic calculations for the 1s pho-

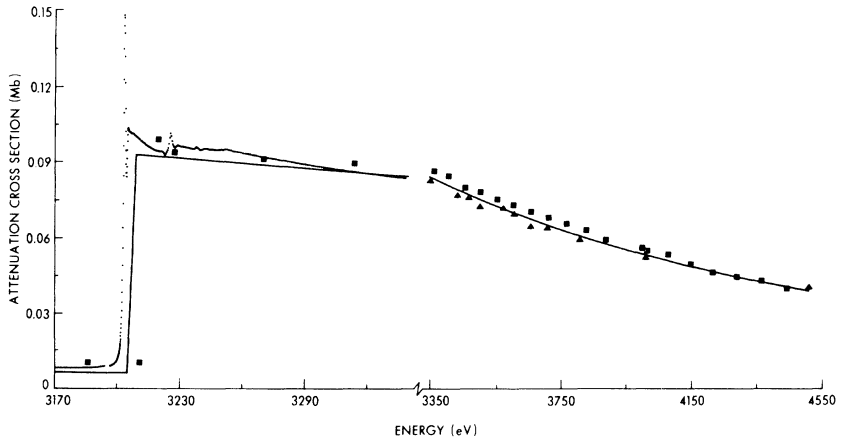

FIG. 4. Argon x-ray absorption spectrum scanned (dots) and discrete data (triangles) from this study are compared with previous measurements (Ref. 7) (squares) and hydrogenic calculations (solid line).

toionization cross section by Manson and Inokuti[23,24] who used Herman-Skillman wave functions for atoms $8 \leq Z \leq 30$ predict a near-threshold (1 to 3 Ry) structure with significant departures from a smooth hydrogenic behavior and appreciable Z dependence. For argon their calculated $1s$ cross section reaches a peak 40 eV above threshold, then decreases to a shoulder at about 135 eV above threshold and continues to decrease smoothly thereafter. The slope from 40 to 135 eV above threshold is steeper than the following decreasing slope. Younger[25] has repeated the calculation for argon using Hartree-Fock wave functions and predicts the $1s$ cross section to peak 15 eV above threshold with similar qualitative behavior as the work of Manson and Inokuti. Both of these calculations are less successful in accounting for the magnitude of the cross section than is the simple hydrogenic model. Departure of the calculated cross section from a monotonic behavior is due to energy dependence of the continuum amplitude at the nucleus arising in the normalization process. It seems possible that a more detailed calculation using accurate wave functions might be able to reproduce this near-threshold behavior. Such an investigation might be a useful precursor to attempt to account for the much more complex behavior at and beyond the first double threshold.

Additional fine details evident in Fig. 4 are shown more clearly on the expanded scales in Fig. 5. All energy scales are adjusted so that the onset of the one-electron continuum is at 3206.0 eV.[26] A local scale is also shown relative to this starting point taken as zero. In the region 18 to 35 eV above the previously specified origin, one sees features in general agreement with prior observations but with improved resolution and contrast (Fig. 5). As a guide to help identify the structures in this region, we have made nonrelativistic Hartree-Fock calculations[27] for a number of configurations. The calculated center of gravity energies are listed in Table I, together with the energy separations of the configurations from the calculated series limit $\underline{1s}\,^2S_{1/2}$ and some relevant excited levels from potassium optical spectra as would be expected to resemble this spectrum in the $Z+1$ approximation. Most of the calculated energy positions are also included in Fig. 5 and arranged (where possible) as series shown *above* the observed spectrum. We also indicate the $Z+1$ approximation by noting *below* the spectrum positions of excited states in the potassium optical spectrum relative to the $K(\mathrm{I})\ 3p^6\,{}^1S_0$ limit which is placed in coincidence with the Ar $\underline{1s}$ threshold at 3206 eV. At the present time it appears that the $Z+1$ approximation retains a certain utility.

The features designated A and B in Fig. 5 are plausibly associated with discrete transitions to the neutral configurations $\underline{1s\,3p}4s^2$ and $\underline{1s\,3p}4p^2$, respectively, and possibly with the $\underline{1s\,3p}4s\,\overline{3d}$ configuration occurring in the same region. In a single-configuration model the $\underline{1s\,3p}4p^2$ can be populated by shake up while the other two can be populated by the relatively weaker conjugate shake-up process. The intensity of the three transitions will be modified by configuration mixing. This is in qualitative agreement with the relative sizes of the features A and B and leads us to suggest associating the labeled features with the first (and most prominent) members of their respective series.

The small peak at feature C is in good alignment with the configuration $\underline{1s\,3p}4p\epsilon p$ which is the first member of the single-ion series above the $\underline{1s}$ threshold which conforms to the above indicated rule. The origin of feature D, the weak window, is not clear, but we suggest that it may be due to the mixing of $\underline{1s\,3p}5p\epsilon p$ and $\underline{1s\,3p}5s\epsilon s$ configurations of the

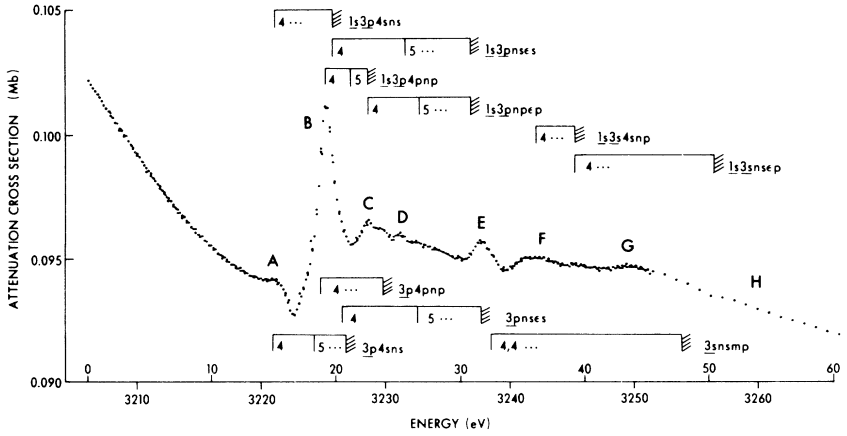

FIG. 5. Expansion of suprathreshold structure from Fig. 4.

TABLE I. Energy estimates for doubly excited KM term values as obtained from nonrelativistic Hartree-Fock calculations and as estimated in the $Z+1$ approximation using potassium optical data.

Argon configuration	Center for gravity energy (a.u.)	Energy above $\underline{1s}$ (eV)	Energy[a] above $3p^6$ (eV,K)	K configuration
ground state	−526.814 827			
$\underline{1s}4p$	−409.484 65	−2.63	−2.73	$3p^6 4p$
$\underline{1s}$	−409.387 87	0	0	$3p^6$
$\underline{1s\,3p}4s^2$	−408.827 62	15.24	14.38–14.64	$\underline{3p}4s^2$
			15.93–16.30	$\underline{3p}4s$
$\underline{1s\,3p}4s\,3d$	−408.756 80	16.90	15.42–18.08	$\underline{3p}4s\,3d$
			18.08–18.62	$\underline{3p}4s\,5s$
$\underline{1s\,3p}4p^2$	−408.683 81	19.15	17.97–19.08	$\underline{3p}4p^2$[b]
$\underline{1s\,3p}4s$	−408.650 96	20.05	20.15–20.64	$\underline{3p}4s$
$\underline{1s\,3p}4p\,5p$	−408.612 191	21.10		
$\underline{1s\,3p}4p$	−408.556 08	22.63	22.72–26.66	$\underline{3p}4p$
$\underline{1s\,3p}5s$	−408.443 83	25.68	26.36–26.66	$\underline{3p}5s$
$\underline{1s\,3p}5p$	−408.410 606	26.58		
$\underline{1s\,3p}$	−408.258 31	30.73	31.63	$\underline{3p}$
$\underline{1s\,3s}4s\,4p$	−408.063 75	36.02	32.55	$\underline{3s}4s\,4p$[c]
$\underline{1s\,3s}4s$	−407.938 165	39.43		
$\underline{1s\,3p^2}4s\,3d\,4p$	−407.901 58	40.43		
$\underline{1s\,3p^2}4s\,4p$	−407.621 56	48.05		
$\underline{1s\,3s}$	−407.545 94	50.10	47.82	$\underline{3s}$
$\underline{1s\,3p^2}4p^2$	−407.487 41	51.69		
$\underline{1s\,3p^2}$	−406.577 564	76.25		
$\underline{1s\,3s\,3p}4p$	−406.455 114	79.77		

[a]C. Corliss and J. Sugar, J. Phys. and Chem. Ref. Data 8, 1109 (1979).
[b]M. W. D. Mansfield, Proc. R. Soc. London, Ser. A 346, 539 (1975).
[c]Reference 26.

singly charged ion with the underlying continuum. Mansfield[28] observed a somewhat similar window in the K(I) optical absorption at 336 Å and tentatively classified this feature as $\underline{3s}4s\,4p$ with possible mixing with the $\underline{3p^2}4s\,3d\,4p$ configuration. We believe that the Fano shaped resonance feature E is mainly due to the opening of the $3s$ channel, namely, the neutral $\underline{1s\,3s}4s\,4p$, but the threshold of the $\underline{1s\,3p}$ double ion is also in close coincidence with this feature. In the local energy region 38–48 eV there are many possible final states, a few of which are indicated in Table I. The absence of any prominent feature does not permit even a suggested identification. The break at feature H at about 3256 eV could be the threshold of the double-ion $\underline{1s\,3s}$ or the single-ion shake off $\underline{1s\,3p^2}4p^2$, we return to this feature in Sec. VI. However, the single electron cross section itself may also contribute a broad structure in this region as suggested by calculation by Manson and Inokuti.[23]

We have up to the present made no attempt to produce a detailed model for the absorption data. Although the statistical reliability of our data is superior to that used with earlier model calculations,[2,4] we feel that several of the above uncertainties must be resolved before any meaningful model can be constructed.

VI. OBSERVATIONS OF EMISSION SPECTRA

Emission profiles at Ar $K\beta$ energies were acquired for 55 different primary excitation energies between −43 and +400 eV relative to the single- ($1s$) vacancy term value (3613–3606 eV absolute). A spectrum [Fig. 6(a)] typical of those obtained at high excitation energies shows the same three prominent features, traditionally labeled $K\beta_{1,3}$, $K\beta^V$, and $K\beta''$, that are seen under electron bombardment (Fig. 1) with the same instrumentation. However, at excitation energies between ~20 and ~60 eV above threshold the $K\beta''$ feature disappears and only the $K\beta^V$ satellite persists [e.g., Fig. 6(b)]. Between threshold and +20 eV both satellites are absent leaving only the $K\beta_{1,3}$ diagram line [Fig. 6(c)]. Below threshold (i.e., $h\nu<0$) the emission spectra are dominated by various features due to Compton (A), resonant Raman (B), and Rayleigh (C) scatter-

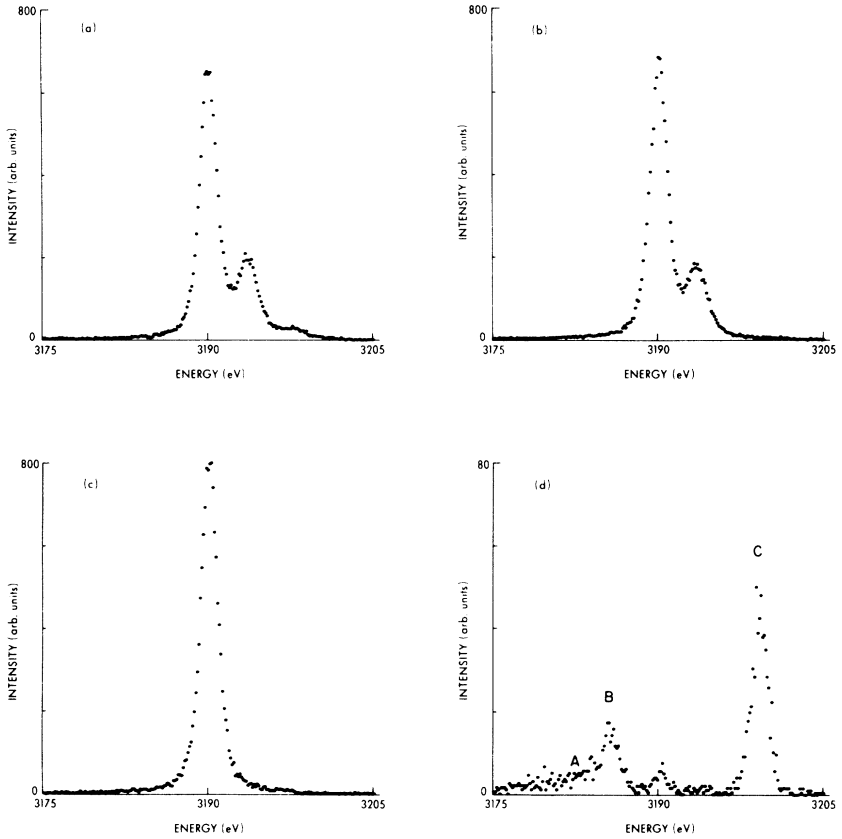

FIG. 6. Sample Ar $K\beta$ emission spectra obtained with incident photon energy at (a) 3281.4 eV, (b) 3245.9 eV, (c) 3213.1 eV, and (d) 3199.2 eV.

ing [Fig. 6(d)] which will be discussed in a subsequent paper. There is, in addition, some residual intensity in Fig. 6(d) at the $K\beta_{1,3}$, $K\beta^V$, and $K\beta''$ energies (the satellites are not clear in the figure) even in the case of nominally subthreshold excitation. This fluorescence is due to excitation by higher harmonics present in the incident beam from the monochromator. The relative amplitude of this contamination is, however, sufficiently small that it can be neglected in analyzing the spectra above threshold. Energy calibration for the reported emission spectra was obtained by detecting the elastic scattered photons at several settings of the primary monochromator far from threshold.

The above qualitative observations combined with our assignment of absorption features from the previous section permit an identification of the origin of the satellites. The presence of $K\beta^V$ only at excitation energies sufficient to create $\underline{1s\,3p}$ hole states confirms this feature as a $\underline{1s\,3p} \rightarrow \underline{3p^2}$ transition. In addition, the appearance of $K\beta''$ at energies above the $\underline{1s\,3s}$ threshold implies that it is due to $\underline{1s\,3s} \rightarrow \underline{3s\,3p}$ transitions.

In order to extract at least semiquantitative information from the emission spectra, we introduce a model spectrum which takes into account the several transitions possible from accessible double-vacancy initial states. Since all such results are to a greater or lesser degree dependent on the choice of model, a thorough description of ours is in order. We first attempted to construct an empirical model from our data with minimal guidance from theory. Initially, the simplest emission spectra, i.e., those exhibiting only the $K\beta$ diagram line, were fit via a nonlinear least-squares routine (using the gradient-expansion algorithm[29]) to an approximation[30] of a Voight peak shape. The Voight peak shape was selected to simulate the convolution of the Lorentzian shape of the emission features with the Gaussian instrumental broadening (mainly due to the electronics). Although the $K\beta_{1,3}$ diagram line is actually a doublet split by ~ 0.2 eV, best fits were obtained with a single Voight peak whose Lorentzian full width at half maximum (FWHM), $\Gamma_L = 1.29$ eV and Gaussian FWHM, $\Gamma_G = 1.26$ eV. The Lorentzian FWHM is noticeably larger than previous values for $K\beta_{1,3}$ life-

time broadening (see for example Ref. 31); this is likely due to crystal contribution which also has a Lorentzian shape. Thus the Γ_L values given here are only upper bounds to lifetime broadening. Monte Carlo tests of the fitting routine confirmed that it is unable to resolve two peaks whose splitting is less than $\sim 30\%$ of their (equal) FWHM's.

The model then was extended to include $K\beta^V$ features. Again the $K\beta_{1,3}$ was represented by a single Voight peak but with constrained values for position (i.e., energy) Γ_L and Γ_G. From one to four additional peaks were included in turn to fit the $K\beta^V$ feature in those spectra with the best statistics. For simplicity, only spectra with evidence of $K\beta^V$ but not $K\beta''$ were used during this phase. To minimize the number of free parameters in the least-squares routine, values of Γ_L for all of the $K\beta^V$ components were assumed to be equal but independent of the corresponding parameter for the $K\beta_{1,3}$ peak; the same assumption was made for Γ_G. Best fits were obtained when three additional component peaks were employed with $\Gamma_G = 1.3$ eV and $\Gamma_L = 1.6$ eV. This implies that the instrumental broadening is constant (as expected) for $K\beta_{1,3}$ and $K\beta^V$, but the multiplet broadening of the multiple-vacancy states is greater (also quite plausible). The energies and relative intensities of the three components are compared in Table II with theoretical predictions.

Although the empirical approach described above produced a plausible model for selected spectra, the fitting program could not obtain consistent results with so many free parameters (three energies, four amplitudes, and two widths) for those spectra where the $K\beta^V$ satellite was weak. Furthermore, to account for spectra with the additional $K\beta''$ feature, which is always relatively dim, more components would be needed. To reduce the number of free parameters the following assumptions were made.

(1) The instrumental broadening was set to $\Gamma_G = 1.3$ eV for all peaks.

(2) The relative amplitudes of the three components of $K\beta^V$ were held constant and equal to the statistical ratios obtained using the Burger-Dorgello-Ornstein sum rule.[33] This assumption is supported by the good agreement between the experimental ratios in Table II and statistical predictions.

(3) The energy of the low-energy $K\beta^V$ feature ($^1P \rightarrow {}^1S$), which is weak and close to the dominant $K\beta_{1,3}$ line, is held constant. The energies of the other two $K\beta^V$ components ($^1P \rightarrow {}^1D$ and $^3P \rightarrow {}^3P$) were

TABLE II. Comparison of various results on energies and relative intensities for the principal multiplet components of the $KM \rightarrow M^2$ transition array.

	Energy (eV) (intensity)				
$KM_{II,III} \rightarrow M^2_{II,III}$	This paper	Deslattes[a]	Dyall[b]	Asplund[c] Moore[d]	Burger-Dongello-Orstein[e]
$^3P \rightarrow {}^3P$	3.7±0.1	~3.7	~4.1	4.3,2.6[f]	
	(0.64)				(0.60)
$^1P \rightarrow {}^1D$	2.8±0.1	2.8	3.0	2.8	
	(0.29)		(0.33)		(0.33)
$^1P \rightarrow {}^1S$	−1.1±0.3	0.4	1.2	−0.5	
	(0.07)		(0.07)		(0.07)
$KM_I \rightarrow M_I M_{II,III}$					
$^1S \rightarrow {}^1P$	5.9±0.8	3.2	0.9	4.9	
	(0.25)[g]		(0.50)		(0.25)
$^3S \rightarrow {}^3P$	7.9±0.1	5.5	~6.7	8.3	
	(0.75)[g]		(0.50)		(0.75)
$^1S \rightarrow {}^3P$		~6.9	8.6		
			(1×10^{-4})		

[a]Reference 9.
[b]Reference 32.
[c]Reference 11.
[d]Reference 12.
[e]Reference 33.
[f]Initial-state energies calculated by Asplund predict that the $^3P_0 \rightarrow {}^3P_1$ transition is at ~2.6 eV while the other $^3P \rightarrow {}^3P$ transitions are at 4.3 eV.
[g]Constrained (see text).

allowed to vary between spectra for reasons discussed below.

(4) Two additional components ($^3S \rightarrow {}^3P$ and $^1S \rightarrow {}^1P$) were used for $K\beta''$ where again statistical ratios were used to constrain their relative intensities. In some spectra it was also necessary to constrain the low-energy ($^1S \rightarrow {}^1P$) component which again is weak and near the stronger $K\beta^V$ features.

(5) The lifetime broadening Γ_L of all three $K\beta^V$ components were set equal but not constrained, and a separate Γ_L for the two $K\beta''$ components was also obtained from the fitting routine.

Since the lifetime broadening of the various multiple-vacancy transitions is not expected to vary with excitation energy, the best fitted values of $\Gamma_L(K\beta^V)$ and $\Gamma_L(K\beta'')$ provide a test for the above assumptions. We find for all spectra $\Gamma_L(K\beta^V) = 1.6 \pm 0.1$ eV and $\Gamma_L(K\beta'') = 1.7 \pm 0.2$ eV. The energies of the $K\beta''$ components are also compared to theoretical predictions in Table II.

It is implicit in the above model that there are three types of initial states, $\underline{1s}(K\beta_{1,3})$, $\underline{1s\,3p}(K\beta^V)$, and $\underline{1s\,3s}(K\beta'')$. In fact, the double-vacancy states should be divided into three classes: doubly excited neutrals, excited single ions, and double ions. The theoretical predictions in Table II are for double ions only. The presence of one or two electrons in the excited levels changes the multiplet splitting so that, in principle, more components should be included in the model. The existing data cannot support so detailed a model, so we have ignored the multiplet due to the neutral and singly excited species. However by allowing the energies of the multiplet components of the double ion to vary, we can account in an *ad hoc* way for differential screening in initial and final states by the additional bound electrons. Figure 7 displays the best fitted energy positions of the major multiplet components as a function of incident photon energy. The energies of the multiplet components increase steeply with excitation energy near their threshold but not at those incidence energies where the double ions threshold should occur. Thus differential screening appears to be unimportant. The energy shifting of secondary emission features at threshold is undoubtedly due to the contribution of resonant Raman scattering.

The best-fit amplitudes of the three groups of peaks, $K\beta_{1,3}$, $K\beta^V$, and $K\beta''$, were normalized using the current from the radiation monitors integrated over the accumulation time of most emission spectra. Thus normalized fluorescence rates were obtained for several incident excitation energies. These fluorescence rates can be equated to partial cross sections for exciting the appropriate initial states multiplied by fluorescent yields. Figure 8 shows the ratio of the $K\beta_{1,3}$ fluorescence in arbitrary units to

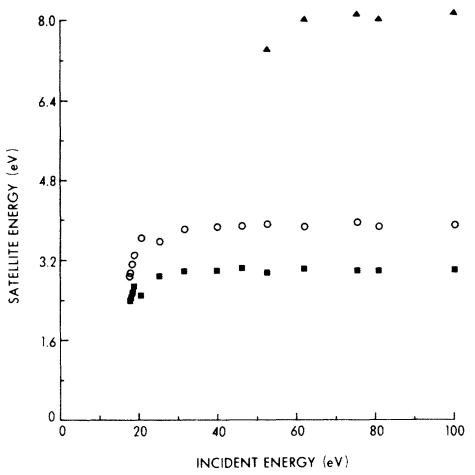

FIG. 7. Emission satellite energy vs incident energy. Both fit energies of $\underline{1s\,3p}\,{}^1P \rightarrow \underline{3p^2}\,{}^1D$ (squares) $\underline{1s\,3p}\,{}^3P \rightarrow \underline{3p^2}\,{}^3P$ (circles), and $\underline{1s\,3s}\,{}^3S \rightarrow \underline{3s\,3p}\,{}^3P$ (triangles) are shown.

the total attenuation cross section μ. Since μ is expected to be dominated by the cross section for photoemission to $\underline{1s}$ single-vacancy ions, Fig. 8 can be interpreted as a measure of the fluorescence yield versus incident photon energy near threshold. Although the scatter previously discussed is again evident, it appears that the fluorescent yield for $K\beta_{1,3}$ is roughly constant or slowly decreasing.

The ratio of $K\beta^V$ and $K\beta''$ satellite intensities to the diagram line intensity versus energy is plotted in Fig. 9. The amplitudes of the three $K\beta^V$ components have been summed as were those of the two $K\beta''$ components. By assuming constant fluorescence yields for the satellite initial states, one can interpret Fig. 9 as a plot of relative partial cross sections.

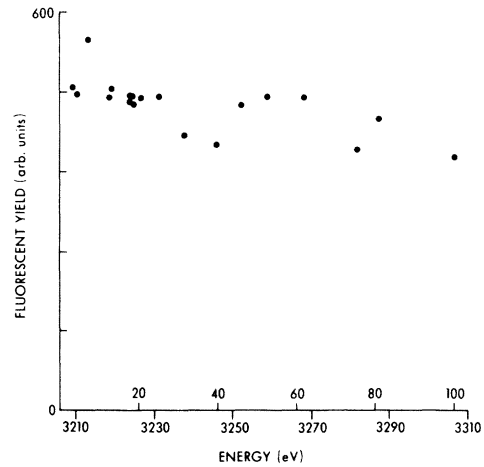

FIG. 8. Ar $K\beta_{1,3}$ fluorescent yield vs energy.

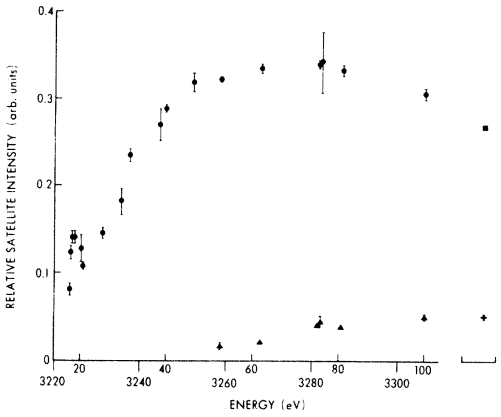

FIG. 9. Relative satellite intensity vs incident energy. Total $K\beta^V$ intensity (circles) and total $K\beta''$ intensity (triangles) relative to the corresponding $K\beta_{1,3}$ intensity are shown vs incident energy. Also shown at right are the relative satellite intensities observed during 10-kV electron bombardment.

The plot of the relative satellite intensities shows several distinct features. First, around 19 eV there is evidence of a resonant production of $K\beta^V$ corresponding to the resonant absorption feature at this energy (see Fig. 5). The emission resonance feature might be more pronounced if the effective energy resolution were not degraded by long-term instabilities in the primary monochromator. Second, the cross section for creation of the $1s\,3p$ initial state is seen to undergo a noticeable increase near 31 eV. This is in good correspondence with the opening of new channels for the creation of the $1s\,3p$ initial state. Third, the plot of cross section for production of the $1s\,3s$ initial state is in apparent contradiction to our identification of absorption features. In the absorption spectra we identified features at energies near 31 eV and above as transitions to $1s\,3s4s\,4p$ and various transitions to excited single ions. However no evidence of $K\beta''$ is found by sensitive fitting procedures in the emission data until energies exceed the Ar^{2+} $1s\,3s$ threshold at $+50$ eV. We feel that an explanation may be that an argon atom with $1s\,3s$ vacancies and loosely bound outer electrons undergoes a Coster-Kronig transition to convert the $3s$ hole to a $3p$ hole before the radiative transition. In particular, the initial $1s\,3s4s\,4p$ excited state can decay by CK to the single ion $1s\,3p4s$ plus a 16-eV electron, using the calculated values in Table I. Similarly, the initial $1s\,3s4s$ single ion can decay by CK to the double ion $1s\,3p$ plus an 8-eV electron. The following decay by radiative transitions in the above two cases would be additional contributions to the $K\beta^V$ complex, which is in accordance with the continuing increase of the $K\beta^V$ relative intensity with photon energy. Further support of the above suggestion is found in the noticeably larger breadth of the absorption feature E in Fig. 5 and the lack of any sharp features thereafter. Needless to say, there are many other $1s\,3s$ neutral and single-ion states that can release an electron by CK to produce $1s\,3p$-like states which will radiatively decay.

The threshold for $K\beta''$ is at $+50$ eV, where the double ion $1s\,3s$ is produced. In Ar^{2+} the weakly bound electrons are absent, and the $3s\rightarrow 3p$ transition has insufficient energy to release a $3p$ electron from Ar^{2+}. Hence the $3s$ hole can decay only by a (slower) radiative process increasing the opportunity for $1s\,3s\rightarrow 3s\,3p$ transitions to occur before $3s\rightarrow 3p$ transitions. Using feature H in Fig. 5 at 3256 eV as the threshold of the $1s\,3s$ $^{1,3}S$ double ion and the final state $3s\,3p$ ^3P average energy of 57.5 eV from Moore,[12] one estimates $1s\,3s$ $^3S\rightarrow 3s\,3p$ ^3P at 3198.5 eV in good agreement with the position of $K\beta''$.

VII. CONCLUSION

Although the initial measurements reported here are in many ways flawed and incomplete, we easily exceeded our intentions for this preliminary study. Our results clearly indicate that fluorescence satellites due to multiple vacancies can be extinguished by the proper choice of excitation energy. Further, we have demonstrated the measurement of at least the most prominent features in the excitation function of these satellites. In addition, we have shown in unprecedented detail an atomic x-ray absorption spectrum, whose intricate structure is suggestive of similar features that have been studied by ultraviolet absorption.[34] This atomic absorption structure also has important implications for molecular and condensed phase structure determination by extended x-ray absorption fine-structure measurement[35] and near-edge structure study.[36] Finally, the combination of absorption and emission spectroscopy is synergistic in that each technique is able to clarify the origin of certain features observed by the other method.

Additionally, more precise measurements of the type described here are expected to reveal additional details. Already our observation of the threshold behavior of $K\alpha$ satellites provided additional data on the creation of KM as well as KL double vacancies. Furthermore, we intend to combine absorption spectroscopy with other secondary detection schemes such as electron spectroscopy. Finally, molecular x-ray emission spectra are often complicated by the superposition of the many nondegenerate single-vacancy transitions with multivacancy satellites. Clearly, the ability to extinguish satellites without affecting diagram transitions may be exploited to

provide data for a more detailed description of the molecular electronic structure.

ACKNOWLEDGMENTS

The authors wish to express their appreciation to the Stanford Synchrotron Radiation Laboratory (SSRL) staff for their assistance. In particular, G. Brown, T. Pate, and J. Cerino provided invaluable aid. Synchrotron radiation time and equipment were provided by SSRL which is supported by the National Science Foundation in cooperation with SLAC and the U.S. Department of Energy. We are also indebted to K. Dyall, M. W. D. Mansfield, and S. Younger for their correspondence and sharing of their unpublished work and to J. Cooper for his interest and many discussions of the contents of this paper. Finally, we would like to thank W. Mehlhorn, D. Shirley, and T. Åberg for helpful comments on the manuscript.

---

[1]R. E. LaVilla, Phys. Rev. A 4, 476 (1971).
[2]L. G. Parratt, Phys. Rev. 56, 295 (1939).
[3]G. Brogren, Nova Acta Regiae Soc. Sci. Ups. 14, No. 4 (1948).
[4]T. Watanabe, Phys. Rev. 139, A1747 (1965).
[5]H. W. Schnopper, Phys. Rev. 131, 2558 (1963).
[6]C. Bonnelle and F. Wuilleumier, C. R. Acad. Sci. 256, 5106 (1963).
[7]F. Wuilleumier, J. Phys. (Paris) 26, 776 (1965).
[8]J. B. Hastings and P. Eisenberger, Fifth International Conference on VUV Radiation Physics, Montpellier, France, September, 1977 (unpublished).
[9]R. D. Deslattes, Phys. Rev. 133, A390 (1964).
[10]R. D. Deslattes, Phys. Rev. 133, A399 (1964).
[11]L. Asplund, P. Kelfre, B. Blowster, H. Siegbahn, and K. Siegbahn, Phys. Scr. 16, 268 (1977).
[12]C. E. Moore, Natl. Bur. Stand. Report No. 467, Washington, D.C., 1949 (unpublished).
[13]A. Bienenstock, Nucl. Instrum. Methods 172, 13 (1970).
[14]H. Winick, Nucl. Instrum. Methods 172, 45 (1980).
[15]J. B. Hastings, B. M. Kincaid, and P. Eisenberger, Nucl. Instrum. Methods 152, 167 (1978).
[16]R. Allemand and G. Thomas, Nucl. Instrum. Methods 137, 141 (1976).
[17]LeCroy model TRA510. (Manufacturers of certain items are identified where it was thought that such identification contributed to completeness in description of our apparatus. Such identification does not imply endorsement nor should it be taken to suggest that the indicated items are necessarily best suited to the applications in which they are used.)
[18]Ortec model 464.
[19]M. Stobbe, Ann. Phys. (Leipzig) 3, 661 (1930); for a recent review, see D. F. Jackson and D. J. Hawkus, Phys. Rep. 70, 169 (1981).
[20]H. Wagenfeld, Phys. Rev. 144, 216 (1966).
[21]U. Fano and J. W. Cooper, Rev. Mod. Phys. 40, 441 (1968).
[22]D. R. Bates and M. J. Seaton, Mon. Not. R. Astron. Soc. 109, 608 (1949).
[23]S. T. Manson and M. Inokuti, J. Phys. B 13, L328 (1980).
[24]S. T. Manson (private communication).
[25]S. Younger (private communication).
[26]R. D. Deslattes, Phys. Rev. 186, 1 (1969).
[27]C. Froese Fischer, J. Comput. Phys. 27, 221 (1978).
[28]M. W. D. Mansfield (private communication).
[29]P. R. Bevington, *Data Reduction and Error Analysis for the Physical Sciences* (McGraw-Hill, New York, 1969).
[30]G. K. Wertheim, M. A. Butler, K. A. West, and D. N. E. Buchanan, Rev. Sci. Instrum. 45, 1369 (1974).
[31]M. O. Krause and J. H. Oliver, J. Phys. Chem. Ref. Data 8, 329 (1979).
[32]K. Dyall (private communication).
[33]F. K. Richtmyer, E. H. Kennard, and J. N. Cooper, *Introduction to Modern Physics,* 6th ed. (McGraw-Hill, New York, 1969), p. 438.
[34]For example, see R. P. Madden, D. L. Ederer, and K. Codling, Phys. Rev. 177, 136 (1969).
[35]E. A. Stern, Contemp. Phys. 19, 289 (1978).
[36]A. Bianconi, S. Doniach, and D. Lublin, Chem. Phys. Lett. 59, 121 (1978).